Trends in
Biochemical Sciences

CellPress
OPEN ACCESS

Review

Structural transport and inhibition mechanism of the mitochondrial pyruvate carrier

Denis Lacabanne [1,4], Jonathan J. Ruprecht [1,4], Maximilian Sichrovsky [1], Lucy R. Forrest [2], Vanessa Leone [3], Sotiria Tavoulari [1], and Edmund R.S. Kunji [1,*]

The mitochondrial pyruvate carrier (MPC), of the SLC54 family of solute carriers, has a critical role in eukaryotic energy metabolism by transporting pyruvate, the end-product of glycolysis, into the mitochondrial matrix. Recently, structures of the human MPC1/MPC2 and MPC1L/MPC2 heterodimers in the outward-open, occluded, and inward-open states have been determined by cryo-electron microscopy (cryo-EM) and by AlphaFold modeling. In this review we discuss the membrane orientation, substrate binding site properties, and structural features of the alternating access mechanism of the carrier, as well as the binding poses of three chemically distinct inhibitor classes, which exploit the same binding site in the outward-open state. These structural studies will support drug development efforts for the treatment of diabetes mellitus, neurodegeneration, metabolic dysfunction-associated steatotic liver disease (MASLD), and some types of cancers.

Highlights

The mitochondrial pyruvate carrier (MPC) is a member of the transporter–opsin–G-Protein-coupled receptor (TOG) superfamily, a large and diverse group of membrane proteins that may share a common evolutionary ancestor.

MPC, an inner mitochondrial membrane protein heterodimer, is critical for cellular energy production in eukaryotes, while it also plays important roles in other major biochemical pathways.

Recent structures of two alternative human MPC heterodimers in different conformational states, with or without inhibitors bound, enable a mechanistic model to be put forward, consolidating decades-worth of biochemical studies.

Structural elucidation of the inhibitory mechanism will enable structure-based drug design for treatment of diseases such as specific malignancies, type 2 diabetes, and metabolic-associated steatohepatitis, for which MPC has been proposed as a drug target.

Physiological role, biochemical properties, and therapeutic opportunities

Eukaryotic cells rely on efficient metabolic pathways to produce ATP via oxidative phosphorylation. A key step in this process is the import of pyruvate by the MPC, an integral membrane protein complex located in the mitochondrial inner membrane. In human cells, pyruvate, the substrate of MPC, is generated primarily by glycolysis in the cytoplasm, but can also be derived from lactate, malate, and gluconeogenic amino acids such as alanine, serine, and cysteine (Figure 1A). Once transported into the mitochondrial matrix by MPC, pyruvate is converted by pyruvate dehydrogenase to acetyl-coenzyme A (acetyl-CoA), which enters the tricarboxylic acid (TCA) cycle. This process ultimately enables cells to maximize ATP production through oxidative phosphorylation, increasing the ATP yield approximately 15-fold compared with lactic acid fermentation (Figure 1A). Alternatively, pyruvate can be converted to oxaloacetate by pyruvate carboxylase, providing anaplerotic input to the TCA cycle, which can be the predominant fate of pyruvate under some cellular conditions [1]. This conversion step is also important in gluconeogenesis, which leads to the synthesis of glucose via the malate/aspartate shuttle (Figure 1A). The TCA cycle leads to the formation of citrate, which can also be exported to the cytosol via the citrate carrier to start *de novo* lipid synthesis. Consequently, MPC is important for multiple physiological processes, including embryonic development, and has been proposed as a pharmacological target for metabolic dysfunction-associated steatohepatitis (MASH, previously known as NASH), specific cancers, alopecia, and neurodegeneration, as reviewed elsewhere [2–6].

Pyruvate was originally thought to diffuse into mitochondria passively [7], but kinetic, sulfhydryl reagent, and inhibitor studies later demonstrated the existence of a specific transport protein [8–11]. However, it took 40 years before researchers identified complexes of small, homologous transmembrane proteins in different species [12,13], subsequently classified as solute carrier family **SLC54** (see Glossary) (https://slc.bioparadigms.org). The functional unit of MPC was shown to

[1]MRC Mitochondrial Biology Unit, University of Cambridge, Keith Peters Building, Cambridge Biomedical Campus, Cambridge, CB2 0XY, UK
[2]Computational Structural Biology Section, National Institute of Neurological Disorders and Stroke, NIH, Bethesda, MD 20892, USA
[3]Department of Biophysics and Data Science Institute, Medical College of Wisconsin, Milwaukee, WI 53226-3548, USA
[4]These authors share first authorship

*Correspondence:
ersk2@cam.ac.uk (E.R.S. Kunji).

https://doi.org/10.1016/j.tibs.2025.11.002

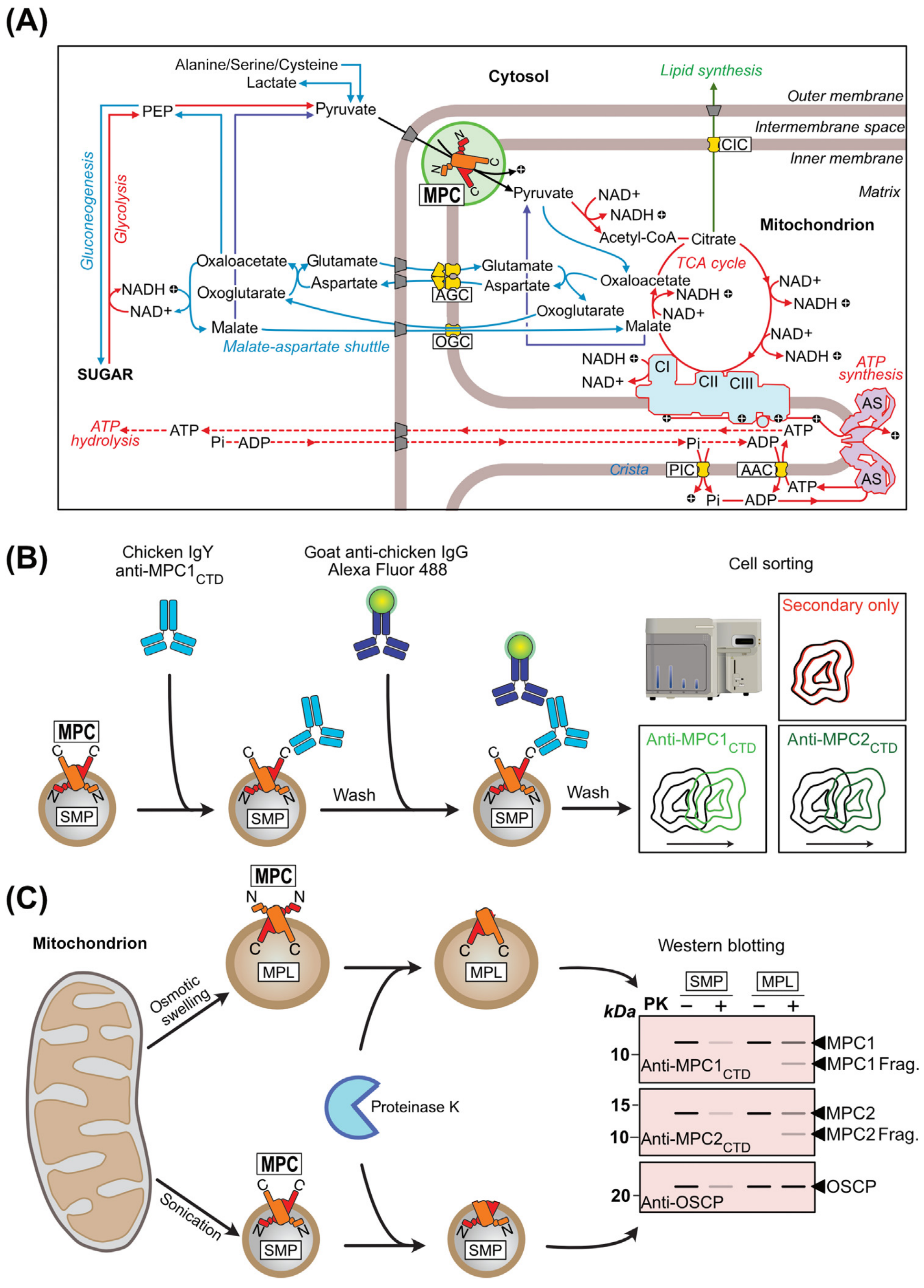

Trends in Biochemical Sciences

Figure 1. Metabolic role and orientation of the mitochondrial pyruvate carrier (MPC). (A) Role of MPC (solute carrier family SLC54) in human metabolism. Pathways are color-coded: glycolysis, TCA cycle, and ATP synthesis and hydrolysis (red), gluconeogenesis and the malate–aspartate shuttle (blue), *de novo* lipid synthesis (green), and malate to pyruvate conversion (purple). The MPC heterodimer is depicted in red and orange with the N and C termini indicated. SLC25 mitochondrial carriers are shown in yellow: aspartate/glutamate carrier (AGC), oxoglutarate carrier (OGC), ADP/ATP carrier (AAC), phosphate carrier (PIC), and citrate carrier (CIC). Respiratory chain complexes I–IV (CI–CIV) and ATP synthase (AS) are shown in light blue and purple, respectively, whereas the voltage-dependent anion channels are shown in gray.

(Figure legend continued at the bottom of the next page.)

Glossary

Compound 7 (C7): a cyano-acrylate inhibitor derivative with greater inhibitory potency (IC_{50} of ~5 nM) than UK5099.

Fiducial markers: proteins fused or attached to a protein of interest to increase its size and to improve its structural features for cryo-electron microscopy and single-particle analysis.

GW604714X: a potent MPC and plasma membrane monocarboxylate transporter inhibitor.

Helical topology: the arrangement of transmembrane alpha-helices within the lipid bilayer.

Inward-open state: the conformation of the mitochondrial pyruvate carrier where the central substrate-binding site is open to the mitochondrial matrix.

Legobodies: large scaffold/nanobody assemblies used to increase the size of a protein for cryo-electron microscopy and single-particle analysis.

Limited-proteolysis experiments: a technique used to study which membrane protein regions are solvent-accessible by cleaving the protein with a protease under limiting conditions.

Mitoglitazone (MTG): a next-generation thiazolidinedione designed to have lower potency for PPARγ.

Mitoplasts: mitochondria that have been stripped of their outer membranes by osmotic swelling, preserving the original orientation of the membrane proteins in the inner membrane (right-side-out orientation).

Nanobodies: single-domain antibodies raised against folded protein epitopes specifically, which aid the structure determination by cryo-EM or X-ray crystallography.

Occluded state: the conformation of the mitochondrial pyruvate carrier in which the binding site is inaccessible from both sides of the membrane.

Outward-open state: the conformation of the mitochondrial pyruvate carrier where the central substrate-binding site is open to the mitochondrial intermembrane space.

Pro-macrobodies: engineered proteins consisting of a specific nanobody fused to maltose-binding protein (MBP) connected through a linker.

SLC54: the solute carrier family of mitochondrial pyruvate carrier proteins, comprising three members (MPC1, MPC1L, and MPC2 in humans) forming the functional heterodimers MPC1–MPC2 and MPC1L–MPC2.

be a heterodimer, both protomers being necessary for pyruvate transport and inhibitor binding [14,15]. In yeast, the Mpc1p/Mpc2p heterodimer is expressed during fermentative growth, whereas Mpc1p/Mpc3p is predominantly expressed under aerobic conditions [16], indicating regulatory diversification in response to metabolic state. In humans, the MPC1/MPC2 heterodimer is expressed in all tissues, whereas MPC1L/MPC2 is found exclusively in the testes of placental mammals for reasons that are currently not understood [17]. Both human MPC complexes have been shown to transport pyruvate and to bind the same inhibitors with similar affinities [15].

Due to its key metabolic role, MPC has become a promising therapeutic target for different conditions, such as MASH [18–22], type 2 diabetes [23], neurodegenerative diseases [24–26], and certain malignancies [27–29]. Several different inhibitors of MPC have been identified over the past decades, and although most have other primary targets, these discoveries have greatly advanced MPC pharmacology (reviewed in [2]). Some of the highest-affinity and best-characterized inhibitors include derivatives of α-cyano-cinnamates, such as α-cyano-β-(1-phenylindol-3-yl)-acrylate **(UK5099)** (50 nM potency) [10,11] and 2-cyano-3-[5-(2-nitrophenyl)-2-furyl]acrylic acid **(compound C7)** (5 nM potency) [15]. A wide variety of lower-affinity inhibitors has been revealed in recent years, including **zaprinast** [30], an inhibitor of cyclic GMP (cGMP)-specific phosphodiesterase (PDE) and a lead compound in the development of sildenafil (Viagra), the anticancer agent lonidamine [31,32], and a range of glitazones, including **thiazolidinediones (TZDs)** [33,34], used to treat type 2 diabetes. The inhibitory potencies of these medically relevant compounds are in the low micromolar range [15], suggesting that their therapeutic benefit may be due, at least in part, to MPC inhibition.

In this review we discuss new molecular insights gained from recently published atomic structures of the human MPC in several conformational states, both ligand-bound and free [35–38]. These advancements are crucial for understanding the molecular mechanism of transport and inhibition and for generating new therapeutic opportunities through structure-based drug design.

Helical topology and orientation in the mitochondrial inner membrane

Following the identification of the MPC proteins [12,13] and the elucidation of the heterodimer as the functional unit [14,15], the number of transmembrane helices of each protomer and the orientation of the heterodimer in the membrane remained unresolved. An earlier **helical topology** study, using labeling of single cysteine MPC variants in isolated mitochondria, had suggested that yeast Mpc1 has two transmembrane helices, whereas Mpc3 has three [16]. The same topology was also proposed for the human orthologs [17]. However, these topologies contradicted secondary structure predictions, hydropathy profiles, sequence similarity, and computational models (reviewed in [2]). The experimentally determined structures of human MPC1L/MPC2 [35] and MPC1/MPC2 [36–38] now show conclusively that each protomer has an N-terminal amphipathic helix and three transmembrane helices.

Submitochondrial particles: inner mitochondrial membrane vesicles formed by sonication of mitochondria; the particles are essentially isolated cristae, meaning that the matrix side of the membrane proteins is now exposed to the outside (inside-out orientation).
Thiazolidinediones (TZDs): PPARγ agonists used in diabetes treatment, with low micromolar potencies for MPC.
UK5099: a well-characterized cyano-acrylate compound that inhibits MPC (IC_{50} ~50 nM) but also the plasma membrane monocarboxylate transporters.
Zaprinast: a phosphodiesterase inhibitor and lead compound for the development of sildenafil (Viagra), known to inhibit MPC with high potency.

Protons are represented as black circles with white plus signs. (B) Antibody-labeling strategy for flow cytometry. Submitochondrial particles (SMPs) prepared from bovine mitochondria were incubated with primary antibodies against the C-terminal domain (CTD) of MPC1 or MPC2, followed by secondary antibodies conjugated to Alexa Fluor 488. Fluorescence labeling was analyzed by flow cytometry. Only specific C-terminal antibodies could label MPC in SMPs, seen by a shift in the particle population. (C) Proteinase K protection assay. Mitoplasts (MPLs) (osmotically swollen mitochondria with no outer membrane) and SMPs were treated with proteinase K. Immunoblotting with antibodies against the C termini of MPC1 and MPC2 revealed differential protease sensitivities, consistent with an MPC topology where the N termini face the intermembrane space and the C termini the matrix. Degradation of oligomycin-sensitivity-conferring protein (OSCP) confirmed the inverted orientation of the SMPs. Based on experiments from Sichrovsky *et al.*, 2025 [35]. Abbreviation: PEP, phosphoenolpyruvate.

Given the altered helical topology, the previously proposed orientation of MPC in the membrane [16,17] also became ambiguous. Based on single-cysteine-labeling, generating small molecular weight shifts, and limited-proteolysis experiments, it had been suggested that the N termini of both protomers are located in the mitochondrial matrix, whereas the C terminus was in the matrix for yeast Mpc1 and in the intermembrane space for yeast Mpc2 [16], as was also observed for human MPC1 and MPC2 [17].

In their structural studies on the human MPC1/MPC2 complex, Liang *et al.* [36], He *et al.* [37], and Sun *et al.* [38] adopted the previously proposed orientation of MPC2 for both protomers, locating both C termini in the intermembrane space. However, these studies do not provide a rationale or experimental support for these decisions. If this orientation were correct, the inhibitors would first need to diffuse through the mitochondrial inner membrane before they could bind to binding sites in MPC. However, most inhibitors have polar or zwitterionic groups, and UK5099 and its derivatives are even negatively charged, meaning that they would have to diffuse across the inner membrane against the membrane potential, making the proposed orientation implausible.

Seeking clarity on this issue, Sichrovsky *et al.* performed an independent investigation into the orientation of MPC in the inner membrane [35]. Flow cytometry data showed that the C termini of MPC1 or MPC2 can be labeled with specific fluorescent antibodies in **submitochondrial particles** in which the matrix side of MPC is out (inside-out) (Figure 1B) [35]. Independently, **limited-proteolysis experiments** with the bovine MPC1/MPC2 complex, which is ~96% identical to the human complex, showed that both C termini are protected in **mitoplasts**, where the orientation of MPC in the membrane is retained (right side-out), but not in submitochondrial particles, where the orientation is inverted (inside-out), indicating that the C termini are located in the matrix (Figure 1C) [35]. Together, these data show that both N-terminal amphipathic helices are located in the intermembrane space, whereas both C termini are in the matrix [35], that is, the opposite orientation from the one proposed earlier [16,17]. Our proposed orientation is compatible with the TIM22-mediated insertion mechanism in the inner membrane, which leaves the N terminus in the intermembrane space, as shown previously for SLC25 mitochondrial carriers [39] and SLC56 sideroflexins [40]. A final point in favor of our proposed orientation is that the inhibitors would only have to pass the voltage-dependent anion channels in the mitochondrial outer membrane to bind to their binding sites in MPC [35]. For all of these reasons, we posit that the N-terminal amphipathic helices are located in the intermembrane space and the C termini in the mitochondrial matrix.

Structures determined by cryo-EM and AlphaFold

More than 12 years after the identification of MPC proteins, four groups, including ours, have independently reported the structures of human MPC1/MPC2 [36–38] and MPC1L/MPC2 [35] in various states by cryo-EM. There are two reasons to explain this delay. The first is that these small and hydrophobic proteins are difficult to express and to purify in a functional state and in sufficient yields. Indeed, the first purification and reconstitution of an MPC heterodimer was published 7 years after their identification [14]. The second reason is that their small sizes and twofold pseudo-symmetric arrangement pose a technical challenge for cryo-EM [41,42], but these limitations can be overcome by increasing the size of the particles by binding additional proteins [35–38] or by generating fusion proteins [38].

All four groups have used **fiducial markers**, which enlarge the particles and improve their alignments in single-particle analysis. The largest fiducial was a 120-kDa **legobody**, which binds to the C terminus of MPC1 (total ~46 kDa) [37]. The authors report an overall resolution of 2.83 Å, but this number primarily reflects the rigid core of the legobody. Using the resolution values at the atom positions, the resolution range is 2.9–3.3 Å for MPC1 (with bound legobody) and 3.3–

3.7 Å for MPC2 (free), emphasizing the importance of reporting the resolution range of the target protein separately. The smallest fiducial was a **nanobody** (~14 kDa) [36], which introduces an asymmetrical feature but results in only a minor increase in weight (total ~40 kDa). Consequently, large datasets were required to achieve a reported resolution range of 3.0–3.7 Å. The cryo-EM maps were globally sharpened with a high temperature factor to restore the high-resolution components, leading also to noise amplification, which is apparent in the deposited cryo-EM maps. Interestingly, the raw half-maps show density for the N-terminal amphipathic helix of MPC1, but this feature weakens when global sharpening is applied, and is missing from the final models. This highlights the variable signal-to-noise ratio that can exist across cryo-EM maps and the need to consider localized sharpening and multiple maps for model building [43]. Sichrovsky *et al.* used **pro-macrobodies** [44] as fiducial markers (~58 kDa) to solve the structure of the MPC1L/MPC2 heterodimer (total ~83 kDa) with a resolution range of 3.2–3.7 Å [35]. In this study, AlphaFold 2.0 multimer was also used to generate various conformational states for both MPC1/MPC2 and MPC1L/MPC2 heterodimers (Box 1), which agreed well with the experimentally determined structures of specific states [35]. Sun *et al.* adopted an alternative approach by creating fusion proteins of both MPC1 and MPC2 [38]. They fused maltose-binding protein to MPC1 via a flexible linker, and a DARPin (designed ankyrin repeat protein) to MPC2 via a rigid helical linker. The DARPin is known to bind maltose-binding protein, and both components interact to generate a fiducial marker suitable for cryo-EM analysis, which they reported to be in the resolution range of 3.3–3.6 Å. Despite differences in particle sizes, particle numbers, and computational approaches, the resolution ranges and density map features are very similar (Figure 2A–D). We have argued that the modest resolution of these maps simply reflects the natural properties of MPC, having flexible N-terminal amphipathic helices and a highly dynamic transporter domain [35]. When comparing related states, the structure backbones overlay fairly well (Figure 2E–G). Any differences in the reported structures may thus reflect disparities in modeling and interpretation.

Overall, the structures confirmed the heterodimeric assembly of MPC [35–38], as proposed previously [14,15]. For the earlier outlined reasons, we will use our proposed orientation as the basis for interpreting these structures. Each protomer consists of an N-terminal amphipathic helix, a short linker helix, and three transmembrane helices (H1, H2, and H3), all connected by small loops (Figure 3A). The short loop connecting transmembrane H1 and H2 contains a 3_{10}-helix, whereas transmembrane H3 extends beyond the membrane surface into the mitochondrial matrix. The transmembrane helices are arranged symmetrically around a central twofold pseudosymmetry axis, forming a narrow, barrel-like structure with a water-filled cavity exposed to the intermembrane space or matrix, depending on the state. The N-terminal and linker helices are amphipathic, flexible, and lie on the outer leaflet of the inner membrane (Figure 3A) [35]. In MPC2, these amphipathic helices adopt a helix–turn–helix motif stabilized by polar interactions, disrupting the overall pseudosymmetry because the N termini point in the same direction [35].

The transmembrane helical arrangement is a hallmark of members of the transporter–opsin–G-protein-coupled receptor (TOG) superfamily to which MPC belongs [45], which also includes the plant SWEET transporters [46], the bacterial semiSWEET transporter [47], the lysosomal cystine transporter [48], the KDEL receptor [49], and the G-protein-coupled receptors [45,50].

Conformational mechanism and substrate coordination

The recently solved MPC structures provide critical insights into the conformational changes required for the substrate to be transported from one side of the inner mitochondrial membrane to the other. As with other transport proteins, substrate binding to MPC is expected to promote a series of conformational changes to alternate access to the binding site from one side of the membrane to the other. These conformational changes, from an **outward-open state** to an **inward-open state,** proceed

Box 1. Inferring transport mechanisms from sequence-guided AlphaFold ensembles

To move beyond the static snapshots provided by cryo-electron microscopy (cryo-EM), we employed a computational strategy [32] to explore the full conformational landscape of the heterodimeric mitochondrial pyruvate carrier (MPC) (Figure I). Since the models were generated in the apo form, they are not influenced by biases from inhibitor or nanobody binding, which can stabilize specific conformations in cryo-EM reconstructions. Standard AlphaFold-Multimer (v2) modeling of the MPC heterodimer yields only one dominant conformation, reflecting the strongest coevolutionary signal from the input multiple sequence alignment (MSA). To sample alternative states, we varied the number and diversity of sequence homologs included in the MSA. This alters the set of coevolving residue pairs and, in turn, the pair representation used by AlphaFold, enabling access to a broader ensemble of predicted structures. However, since AlphaFold lacks a physical energy model, many resulting conformations may not be realistic. To address this, we applied physics-based scoring metrics. For the MPC heterodimer, we used ProQDock, which is particularly suited for assessing interface quality in complexes.

After identifying energetically plausible conformations, we needed to quantify and organize diversity within the ensemble. When endpoint structures are unavailable for direct comparison (e.g., by root mean square deviation, RMSD), it becomes essential to define a metric that captures the specific conformational change of interest. This could be a distance, an angle, or another structural descriptor, depending on the biological question. In our case, we probed the alternative access mechanism of a transporter and used a coordination number to describe how the two protomers pack together along the conformational transition. This simplified descriptor effectively captures whether the pathway is open or closed, and remains easy to interpret since higher values indicate tighter packing and a more closed state. Once we have a metric describing the conformational change, how can we use it to identify representative structures that best capture key states along the mechanism? We addressed this by partitioning the conformational space using K-medoids, a clustering method that assigns representative structures as centers of Voronoi-like regions. Unlike grid-based discretization, which often includes sparsely populated regions, K-medoids naturally focus on densely sampled areas. This method also offers precise control over the number of resulting microstates while preserving interpretability, since each center corresponds to a real structural model. This strategy allowed us to reduce the complexity of the conformational ensemble into a small number of representative states. Together, these states describe a plausible mechanism for how MPC transitions between different functional conformations.

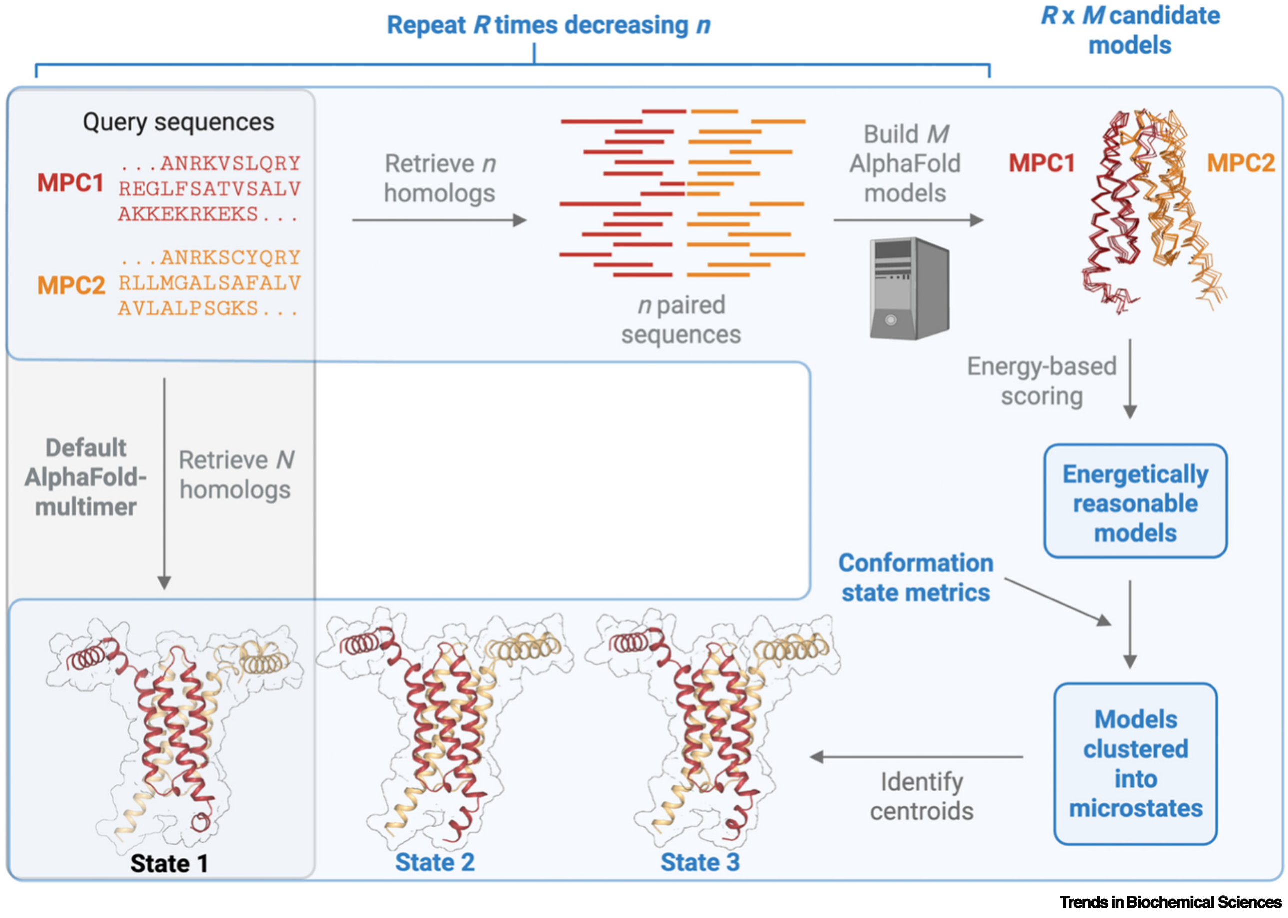

Trends in Biochemical Sciences

Figure I. Workflow for exploring the full conformational landscape of the heterodimeric mitochondrial pyruvate carrier (MPC).

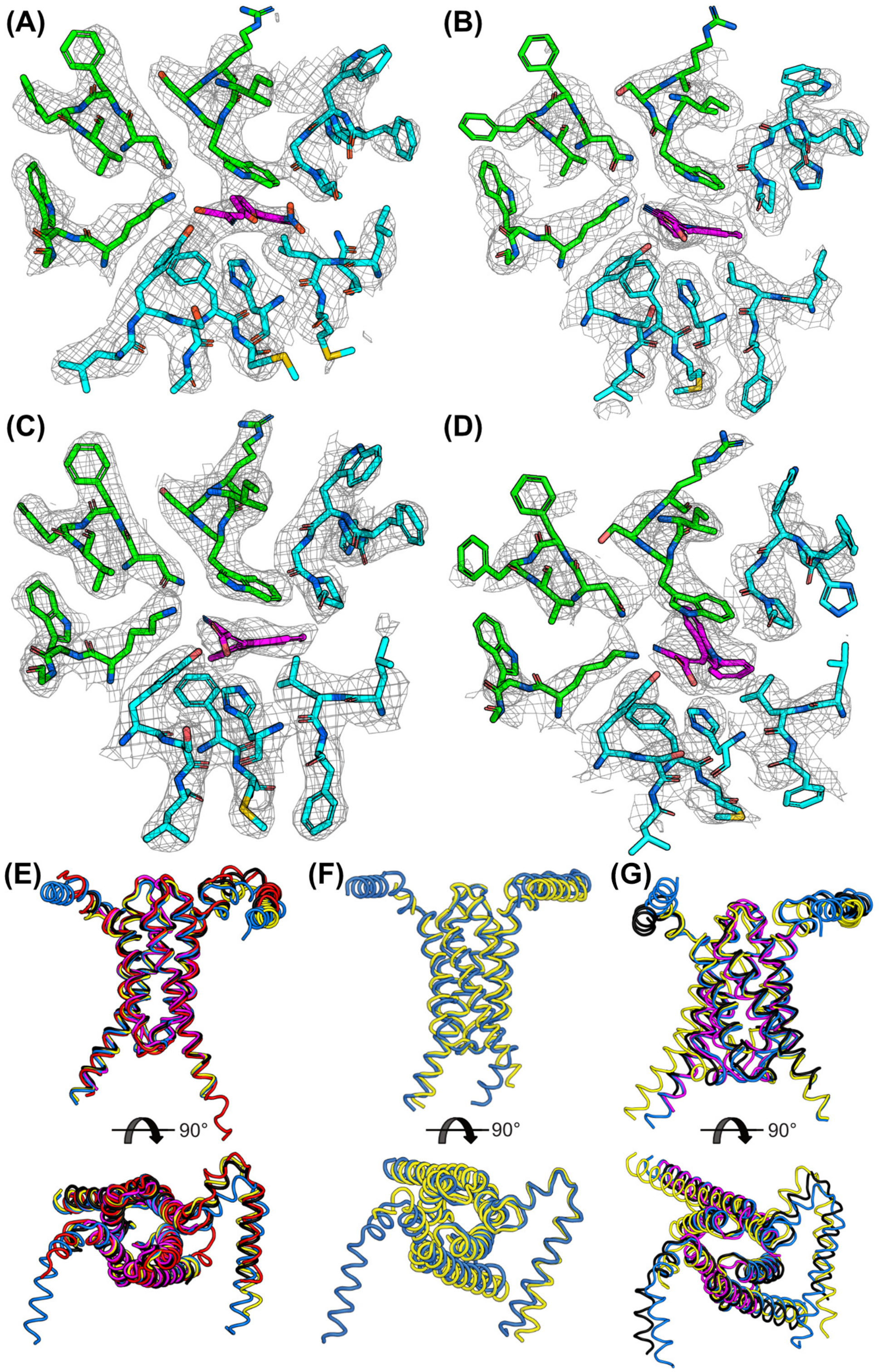

Trends in Biochemical Sciences

(See figure legend at the bottom of the next page.)

through an **occluded state** in which the binding site is inaccessible on both sides of the membrane (Figure 4). A few snapshots of this process have now been revealed.

He and colleagues report an inward-open state of MPC1/MPC2 in the presence of pyruvate (PDB: 9mny). The cryo-EM map shows a density feature close to K49 (MPC2), which cannot be accounted for by the protein, and was modeled putatively as pyruvate [37]. However, the authors note that the density features are insufficient to assign the orientation of the substrate (Figure 3B). As modeled, pyruvate forms a salt-bridge interaction with K49 (MPC2), but is too distant from other residues to make polar interactions. Furthermore, the density feature is also weaker compared with the density of the surrounding residues, suggesting a low occupancy. Given our proposed orientation, it is possible that this inward-open structure captures pyruvate in the process of being released into the mitochondrial matrix (Figure 4D). Sun *et al.* [38] also report an inward-open state of MPC1/MPC2, stabilized by a V74W mutation (MPC2) in the presence of pyruvate. Whilst the amphipathic helices for MPC1 and MPC2, and the C-terminal end of TM3 for MPC2 are absent from the model, the overall model is similar to that of He *et al.* – overall root mean square deviation (RMSD) 1.3 Å for backbone atoms – but there is no bound pyruvate.

Liang *et al.* report a structure of MPC1/MPC2 in an occluded state, which was also generated in the presence of pyruvate (PDB: 9knx) [36]. They describe a small pocket, close to H84 (MPC1) and K49 (MPC2), suggesting that it might be the binding site of pyruvate, but in their modeled structure they have not considered hydrogen atoms. This pocket disappears when hydrogen atoms are added to the protein model (Figure 3C). Thus, it seems that the captured state is not the substrate-bound occluded state (Figure 4C), but possibly an apo occluded state (Figure 4G).

Sichrovsky and colleagues also attempted to determine a structure for MPC1L/MPC2 in the pyruvate-bound state, but they did not observe a bound substrate either [35]. Therefore, they used an AlphaFold multimer to generate numerous conformations of both MPC1/MPC2 and MPC1L/MPC2, covering all states from the outward-open to the inward-open state, including the occluded state (Box 1). The occluded state contains a partially open cavity in the center of MPC, which can accommodate the pyruvate upon minor binding site rearrangement during induced-fit docking (Figure 3D). The bound substrate forms interactions with key residues, such as H86 (MPC1L) and K49 and N100 (MPC2). These interactions were validated by transport assays and pyruvate binding studies with single-alanine-replacement mutants, showing that H86 (MPC1L) and K49 (MPC2) are both essential for pyruvate binding [35]. K49 and N100, but not H84 (H86 in MPC1L), had previously been proposed as important for pyruvate and inhibitor binding in MPC1/MPC2 [51].

Transport studies in isolated mitochondria have shown that pyruvate transport is driven by the pH gradient (ΔpH) across the inner membrane [8–10], but is unaffected by the membrane potential [9], indicative of an electroneutral transport mechanism. The ΔpH dependency of transport was independently confirmed using liposomes with reconstituted yeast or human MPC heterodimers

Figure 2. Structural comparison of binding pockets, conformations, and helical arrangements. (A–D) Details of the cryo-electron microscopy (cryo-EM) maps with structural models showing the binding pocket of UK5099 or compound 7. (A) Structure from Sichrovsky *et al.* [35] (PDB: 9giv; EMD-51378) of MPC1L/MPC2 with bound Compound 7 (C7) (purple). (B) Structures of MPC1/MPC2 with bound UK5099 (purple) from He *et al.* [37] (PDB: 9mnx; EMD-48442), (C) from Liang *et al.* [36] (PDB: 8yw8; EMD-39625), (D) from Sun *et al.* [38] (PDB: 9o9s; EMD-70348). MPC2 is colored green and MPC1 or MPC1L cyan. (E–H) Overlays of MPC models, comparing the same conformational states from Sichrovsky *et al.* (black), He *et al.* (red), Liang *et al.* (yellow), Sun *et al.* (magenta) and AlphaFold models (blue) [35]. (E) Outward-open or inhibited state, with models from Sichrovsky *et al.* (9giv) [35], He *et al.* (9mnx) [37], Liang *et al.* (8yw8) [36], Sun *et al.* (9o9s) [38] and AlphaFold [35]. (F) Occluded state with structures from Liang *et al.* (9knx) and AlphaFold [35]. (G) Inward-open apo state from Sichrovsky *et al.* (9gix), Liang *et al.* (8yw6), Sun *et al.* (9o9t) and AlphaFold.

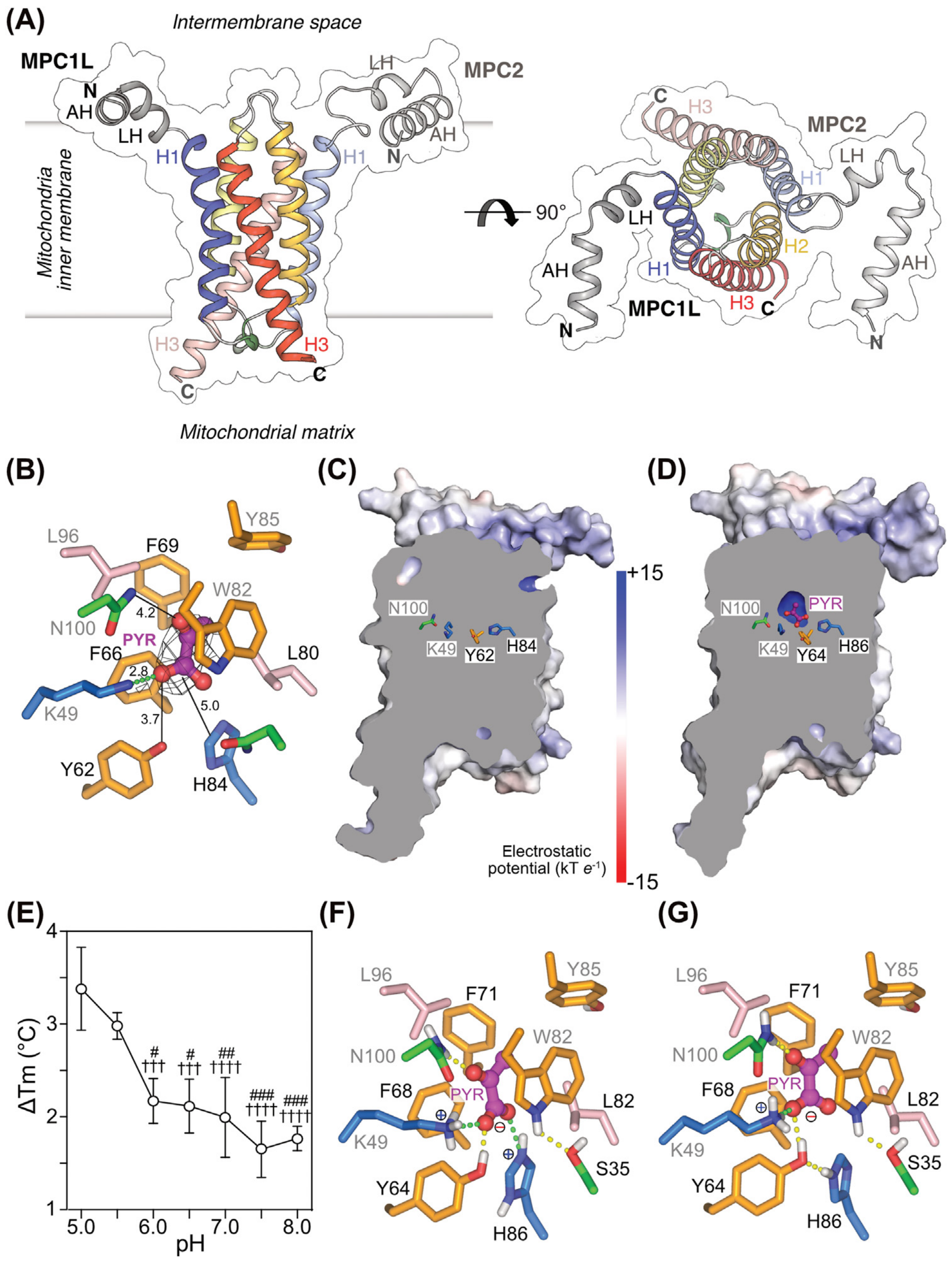

Trends in Biochemical Sciences

Figure 3. Pyruvate binding site of the mitochondrial pyruvate carrier. (A) Lateral (left) and cytoplasmic views (right) of (MPC1L/MPC2. Amphipathic helices (AHs) and linker helices (LHs) are colored gray, transmembrane helix 1 (H1) blue, helix 2 (H2) yellow, helix 3 (H3) red, and the 3_{10}-helix green (PDB: 9giy) [35]. The surface is indicated. Darker and lighter colors and labels are used for MPC1L and MPC2, respectively. (B) View of the putative pyruvate binding site of MPC1/MPC2 (PDB: 9mny). Amino acids in the vicinity of pyruvate are colored according to the Zappo color scheme, and labeled, black for MPC1 and gray for MPC2. The salt-bridge between K49 and pyruvate is shown as a green dashed line with the distance in Å. Thin black lines indicate distances to other residues. (C) Slice through the occluded state structure (PDB: 9knx) with the surface colored by electrostatic potential, as indicated by the color ramp. Potential substrate-binding site residues are also indicated. (D) Slice through the binding site of an AlphaFold model of the occluded state for MPC1L/2 with bound

(Figure legend continued at the bottom of the next page.)

[14,15]. Interestingly, pyruvate binding was observed to be pH-dependent, exhibiting strong binding at low pH and weak binding at high pH (Figure 3E) [35]. The transition occurs around pH 6, which could explain the involvement of H86 (MPC1L), which has a similar pKa [35]. Indeed, docking studies support a role for H86 (MPC1L) in the pH dependence of pyruvate binding. At low pH, protonated H86, together with K49, binds pyruvate via ionic interactions, whereas the hydroxyl group of Y64 and amide group of N100 are predicted to provide additional hydrogen bonds (Figure 3F). When H86 is neutral, it forms a hydrogen bond with Y64 rather than with pyruvate, potentially releasing the substrate from the binding site (Figure 3G) [35]. The same binding arrangement could occur in MPC1/MPC2, where the equivalent residue is H84 in MPC1.

A model of the ΔpH-dependent pyruvate transport cycle

Combining the mechanistic and structural information, we propose the following ΔpH-dependent alternating access mechanism for MPC [35]. In this mechanism, the transport steps are fully reversible and occur under the influence of thermal energy, following similar principles as those developed for the mitochondrial ADP/ATP carrier [52] (Figure 4). In the outward-open state (Figure 4A), the binding site is exposed to a local microenvironment, which could have a pH <6 through the proton-pumping activities of the respiratory chain [53,54]. Pyruvate generated by glycolysis in the cytosol enters the central cavity, where the positively charged K49 is located. Upon binding, the negatively charged carboxylate group of pyruvate can shift the pKa of the H86, facilitating proton binding to the histidine, explaining the coupling mechanism (Figure 4A). The ability of histidine to shift its pKa depending on its microenvironment has been observed in different proteins [55–57]. Interactions with pyruvate may bring K49 on MPC2 and H84/H86 on MPC1/MPC1L closer (Figure 4B), triggering the transition to the pyruvate-bound occluded state by lowering the energy barrier (Figure 4C). As the conformational changes progress, the binding site becomes exposed to the higher pH environment of the mitochondrial matrix, possibly enabling H84/H86 deprotonation (Figure 4D) and pyruvate bonding rearrangement, leading to its release (Figure 4E). Pyruvate is then converted to acetyl-CoA. To reset the transporter, the inward-open apo state (Figure 4F) would then transition to the apo occluded state (Figure 4G), and subsequently to the apo outward-open state for another round of transport (Figure 4H).

We further hypothesize that both the inward- and outward-open states are energetically accessible, as required for an alternating access mechanism, but that there is a bias toward the outward-open state in resting conditions because it has more inter-subunit contacts, representing a lower energy state [35]. The inward-open state, representing a higher energy state, can be reached through pyruvate and proton binding, which lowers the energy barrier. Similar conformational selection, depending on substrate and ion binding, has been mapped in other transporters using electron paramagnetic resonance data [58–60]. Moreover, these principles agree with the known transport properties of MPC and its proposed orientation in the inner membrane (Figure 1). This orientation is further supported by the observation that the cavity in the outward-open state is narrow (Figure 4A), facilitating the electrostatic attraction of pyruvate to the positively charged site and reducing the entropic cost. In the inward-open state, a substantial widening of the water-filled cavity and binding site occurs, expediting the release of pyruvate into the matrix (Figure 4D,E). In conclusion, pyruvate transport depends on the ΔpH, driven by a shift from a low to high pH, but not on the membrane potential, since no net charge is translocated (Figure 4A–E) [8–10,35].

---

pyruvate. Key residues and surface electrostatic potential are shown as in (C). (E) pH-dependency of pyruvate binding to wild type MPC1L/MPC2 determined by thermostability shift assays (*n* = 4). ††† *P* <0.001, †††† *P* <0.0001 compared with ΔTm at pH 5.0, # *P* <0.05, ## *P* <0.01, ### *P* <0.001 compared with ΔTm at pH 5.5. (E,F) Docking studies of pyruvate (PYR) in the representative occluded state model of MPC1L/MPC2, with H86 either protonated (F) or neutral (G). Residues are colored according to the Zappo color scheme, with salt-bridge and hydrogen bond interactions shown as green and yellow dashed lines, respectively. (E–G) results from Sichrovsky *et al.* [35].

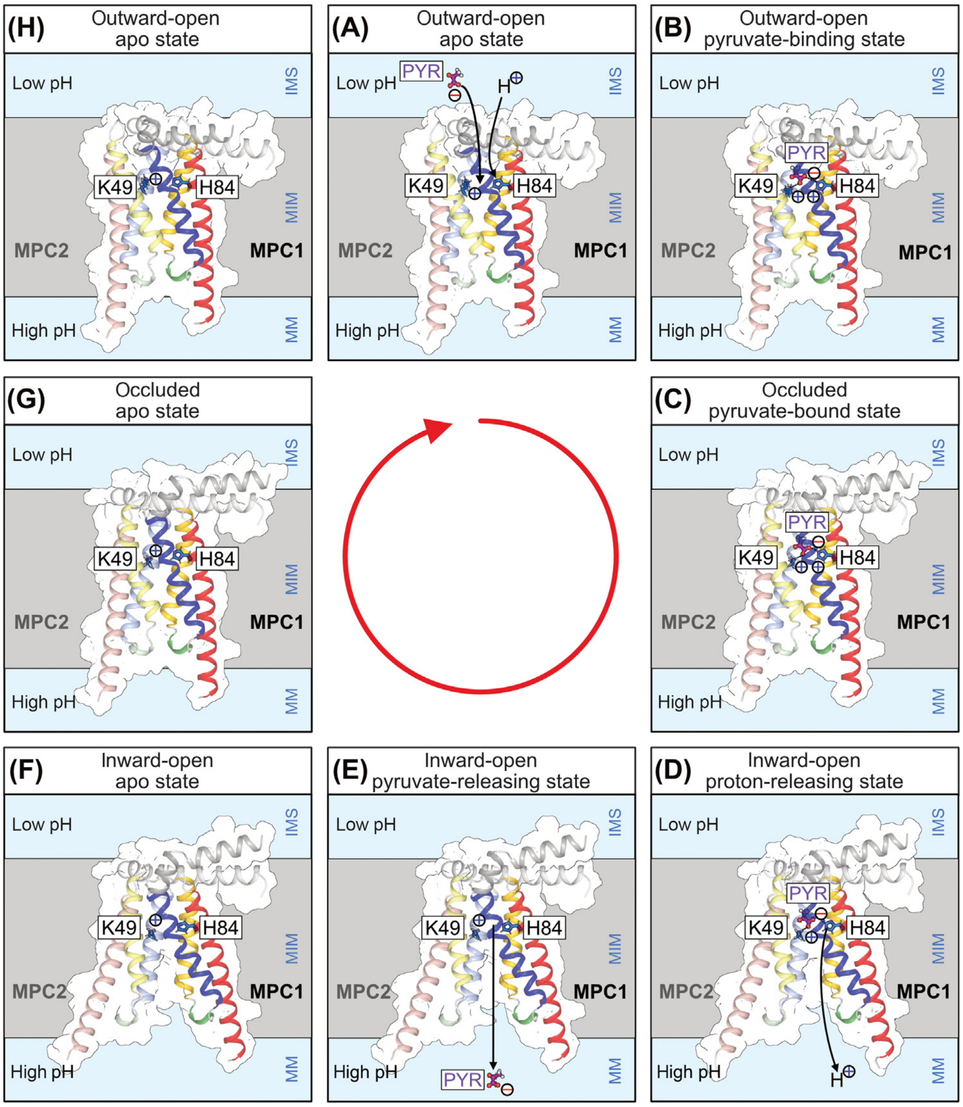

Trends in Biochemical Sciences

Figure 4. Proposed transport cycle of the mitochondrial pyruvate carrier (MPC). (A–H) Lateral views of the different states in the transport cycle of human MPC1/MPC2, starting top middle (A). Amphipathic helices (AH) and linker helices (LH) are colored gray, transmembrane helix 1 (H1) blue, helix 2 (H2) yellow, helix 3 (H3) red, and the 3_{10}-helix green. Lighter colors and labels are used for MPC2. The surface outline of MPC is indicated and the mitochondrial inner membrane (MIM) is colored gray. The models were built using AlphaFold-Multimer v2 and pyruvate binding studies [35] and they are orientated according to Sichrovsky *et al.* [35]. The substrate pyruvate (PYR, purple) and the essential residues for pyruvate binding, K49 and H84 (blue), are also shown. Abbreviations: IMS, intermembrane space; MM, mitochondrial matrix.

The structural basis of inhibitor binding

As already noted, MPC is a key protein complex for cellular metabolism and a promising novel target to treat metabolic conditions. The recent MPC structures have determined the binding poses for several inhibitors: UK5099 (PDB: 8yw8 [36]; PDB: 9mnx [37]; PDB: 9mnz [37]; PDB: 9o9s [38]), compound 7 (C7) (PDB: 9giv [35]; PDB: 9mo0 [37]), thiazolidinediones (PDB: 9giy [35]; PDB: 9mnw [37]), and zaprinast (PDB: 9giw [35]) (Figure 5A–C). Whilst the maps reveal the inhibitor binding sites, their resolution is insufficient to model the inhibitor poses unambiguously.

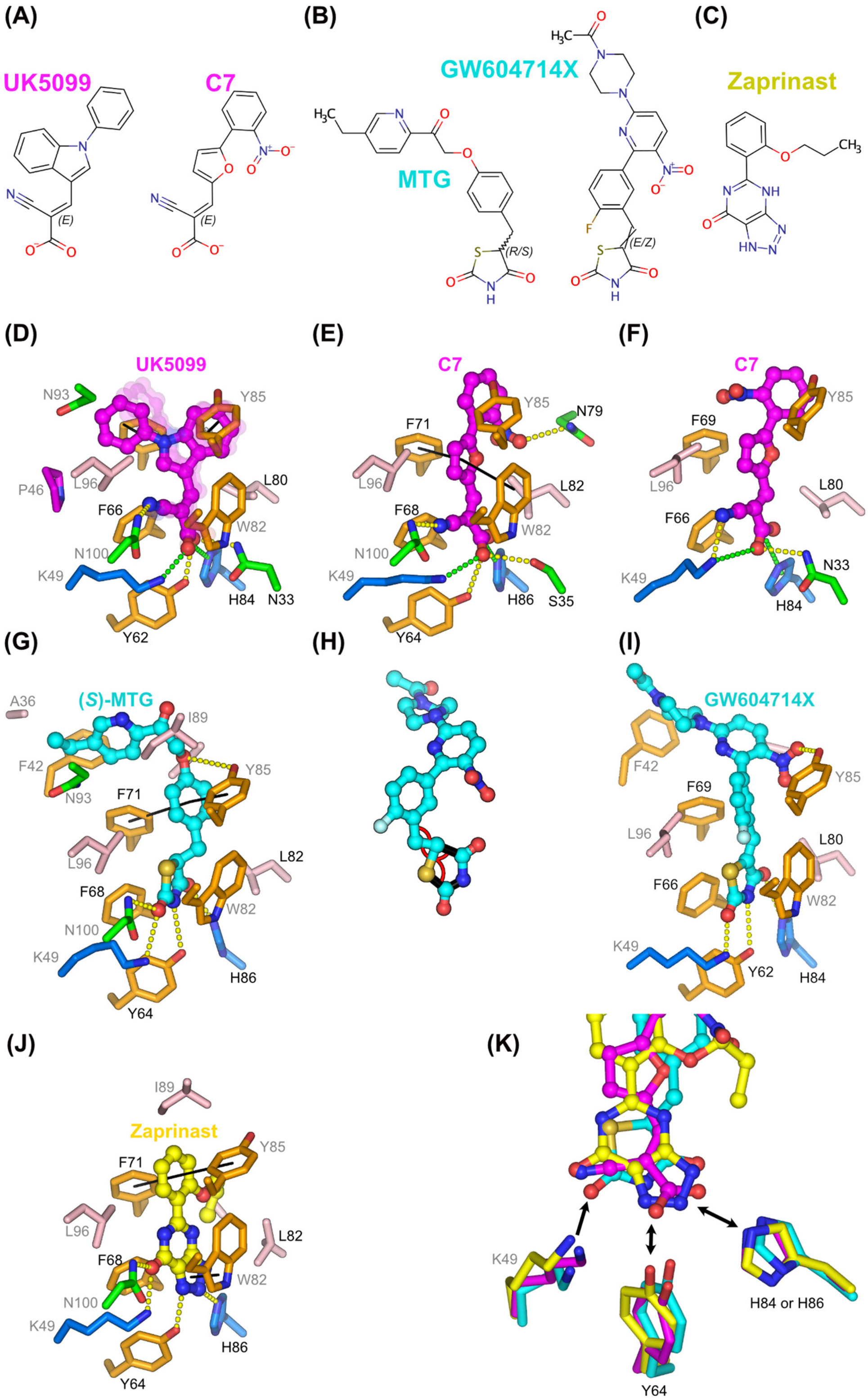

Trends in Biochemical Sciences

Nevertheless, additional information – such as ligand chemistry and ligand–protein interactions, docking analysis, mutagenesis, and binding studies of chemical derivatives – helps to improve their modeling [35]. Multiple structures of the same inhibitors or their derivatives enable cross-validation and assessment of key chemical properties of the inhibitors and binding sites (Figures S1–S4 in the supplemental information online).

Binding of UK5099 and derivatives

Four structures show that UK5099 (Figure 5A) binds to a narrow cleft between MPC1 and MPC2 (Figure 5D), with the cyano-acrylate group facing the bottom of the binding cavity [35–37]. The structures are very similar, with RMSDs of 1.5 Å for backbone atoms, despite the proteins being in different detergent and lipid environments (Figure S1A–D in the supplemental information online). The cyano-acrylate carboxyl forms salt bridges with H84 (MPC1) and K49 (MPC2). N33 and Y62 (MPC1) act as hydrogen bond donors to the carboxyl group, whereas N100 (MPC2) interacts with the cyano group. The phenyl group attached to the indole ring adopts multiple poses, reflecting rotation around the connecting bond and available pocket space (Figure 5D). Some structures indicate π-stacking interactions between the indole ring and Y85 (MPC2) or between the phenyl ring and F71 (MPC1) (Figure 5D). The ligand pose in PDB:9o9s [38] is quite different, as the cyano-acrylate group does not bind as deeply in the pocket and the phenylindole group is rotated by nearly 90° (Figure 2D and Figure S1D).

The high-affinity derivative C7 binds to the same site (Figure 5E,F), with its cyano-acrylate group interacting like UK5099. The furan ring forms π-stacking interactions with F71 (MPC1L) and W82 (MPC2) (PDB: 9giv) (Figure S2A,B) [35]. In one model, the nitro group does not interact with MPC at all (PDB: 9mo0) [37], but in the other it bonds with N79 (MPC1L) (PDB: 9giv) [35], providing a better explanation for the high affinity of C7 [15]. In contrast with earlier proposals [11], there is no evidence for the formation of a covalent bond between a cysteine residue and UK5099 or C7, as was also demonstrated previously [15].

Binding of thiazolidinediones

The MPC structure has also been solved in complex with **mitoglitazone** [61,62] (PDB: 9giy [35]) and **GW604714X** [34] (PDB: 9mnw [37]) (Figure 5B). Their binding sites overlap with those for UK5099 and C7 (Figure 5G and I). Mitoglitazone binds primarily through the TZD ring, which forms hydrogen bonds with Y64 and H86 (MPC1L), and K49 and N100 (MPC2) (Figure S3A in the supplemental information online). The C5 position of the TZD ring is a chiral center with a known propensity to racemize [63]. The cryo-EM map is consistent with either stereoisomer, and both are modeled, each with 50% occupancy and forming similar interactions with MPC. (*S*)-Mitoglitazone is shown in Figures 5G and S3A. The cryo-EM map is insufficient to determine the TZD ring orientation, which was positioned to maximize protein–inhibitor interactions.

Figure 5. Inhibitor binding to the mitochondrial pyruvate carrier (MPC). (A) Chemical structures of UK5099 and its derivative compound C7. (B) Chemical structures of the thiazolidinediones mitoglitazone (MTG) and GW604714X. (C) Chemical structure of zaprinast. (D) View of the binding site for UK5099 (PDB: 8g8w), with salt-bridge, hydrogen bond, and hydrophobic π-stacking interactions as green dashed, yellow dashed, and black lines, respectively. Amino acids are colored according to the Zappo color scheme. The structures of UK5099 in PDB: 9mnx and PDB: 9mnz are shown superposed as semi-transparent ball-and-sticks. (E) View of the binding site for C7 (PDB: 9giv). (F) View of the binding site for C7 (PDB: 9mo0). (G) View of the binding site for (*S*)-mitoglitazone (PDB: 9giy). (H) Structure of GW604714X as deposited at the PDB. Black bonds and red arcs indicate bond lengths and angles, respectively, with a deviation >10 standard deviations (s.d.) from the expected values. (I) View of the binding site for GW604714X after re-refinement. (J) View of the zaprinast binding site. (E–G, I, J) are viewed from the same orientation as (D) and with the same color scheme. (K) View of the pyruvate-mimic region of representatives of all three classes of inhibitors (adapted from Sichrovsky *et al.*, 2025 [35]).

Notably, the racemic nature of the TZD ring may have clinical implications, as stereoisomer-specific pioglitazones have been proposed to exhibit therapeutic benefits with minimal peroxisome proliferator-activated receptor γ (PPARγ) activity, potentially through their action on MPC [21,22].

GW604714X is a TZD with an sp^2-hybridized C5, lacking a chiral center (Figure 5B) [34]. Nevertheless, the C5 double bond can adopt either *E* or *Z* configurations, and is prone to isomerization. The deposited inhibitor structure (PDB: 9mnw) contains several significant bond length and angle deviations, as described in the PDB validation report (doi.org/10.2210/pdb9MNW/pdb), indicating a lack of suitable restraints during model building and refinement (Figure 5H). Both *E* and *Z* configurations of the double bond fit into the density, with the TZD ring flipped by 180°. The *Z* configuration, as remodeled here (Figure 5I and Figure S3B), maximizes protein–inhibitor interactions, and matches the TZD ring orientation observed for mitoglitazone. In this pose, the TZD ring forms hydrogen bonds with residues Y62 and H84 (MPC1) and K49 (MPC2), while the nitro group acts as a hydrogen bond acceptor from Y85. Despite chemical differences beyond the TZD ring, mitoglitazone and GW604714X share an L shape and bind similarly to MPC.

Binding of zaprinast

The only structure for zaprinast (PDB: 9giw) [35] shows that the heterocyclic ring points toward the bottom of the binding pocket, forming hydrogen bonds with Y64 and H86 (MPC1L) and K49 and N100 (MPC2) (Figure 5C,J and Figure S4A in the supplemental information online).

Common principles of inhibitor binding to the MPC

Despite having different chemistries, all three inhibitor classes bind to the same pocket in the outward-open state. The cyano-acrylate groups of UK5099 and C7 provide three closely spaced hydrogen bond acceptors (Figure 5K). The TZD ring of mitoglitazone and GW604714X provides two hydrogen bond acceptors (carbonyl oxygens) and one donor (an amine group). The triazolopyrimidinone ring of zaprinast provides two hydrogen bond acceptors (carbonyl oxygen and one nitrogen) and one hydrogen bond acceptor or donor (second nitrogen). For all three inhibitor classes, these acceptor/donor groups mimic the equivalent groups in pyruvate, interacting with K49 (MPC2) and H84 (MPC1) or H86 (MPC1L), key residues of the substrate-binding site. All three inhibitor classes have a central aromatic group, capable of forming π-stacking interactions with aromatic residues in that region of the MPC. These common binding principles were correctly predicted prior to the structures [15].

Validation of the inhibitor binding poses

To validate the binding pose, He *et al.* [37] and Sun *et al.* [38] used yeast complementation assays on plates [12] with selected single-alanine replacement mutants. However, these indirect assays can be influenced by factors unrelated to substrate binding and transport, such as expression levels, targeting, insertion, folding, and heterodimer formation. Sun *et al.* also carried out isothermal calorimetry measurements for the wild type (Kd 88 nM) as well as K49A and N100A, showing that these mutations abolish UK5099 binding [38].

Liang *et al.* employed pyruvate transport assays with purified protein complexes reconstituted in liposomes [36]. Although they investigated protein incorporation, they did not compare initial transport rates that were normalized to protein reconstitution levels. It is clear, however, that they observed high levels of transport activity for K49A, W82A, and W82D [36], unlike Sichrovsky *et al.*, who found K49 and W82 to be essential for transport [35]. N100A, which does not purify as a heterodimer, as reported by both Liang *et al.* and Sichrovsky *et al.*, also appears to have a high transport activity [36], which is unexpected.

Sichrovsky *et al.* combined alanine mutagenesis of key residues and chemical analogs of MPC inhibitors with thermostability shift assays to assess the binding mechanism directly [35]. They showed that K49, H86, and W82 are important or essential for binding of C7, UK5099, mitoglitazone, and zaprinast, whereas F68 and L82 contribute to C7 binding and Y64 and F68 to zaprinast binding, a finding consistent with structural data. They also performed pyruvate transport assays using MPC reconstituted in liposomes, but the incorporation levels were quantified and used to obtain specific transport rates. This analysis showed that single alanine replacements of the key interacting residues lead to abolishment of transport, in agreement with the structural data [35].

Concluding remarks

The structures of human MPC1/MPC2 [36–38] and MPC1L/MPC2 [35] in several apo and inhibitor-bound states represent a major advance in our understanding of the transport and inhibitory mechanism of MPC. They have clarified the ΔpH-driven pyruvate transport mechanism [35], explaining transport data reported more than half a century ago [8,9]. Importantly, these structures reveal how different inhibitors bind to the same cavity of the outward-open state. Despite chemical differences, all inhibitors exploit similar interactions: polar groups engage with pyruvate binding site residues, while aromatic groups bind in a hydrophobic and aromatic region of MPC [35–38]. Their binding blocks pyruvate from binding and locks MPC in an abortive state [35]. These insights offer a foundation for structure-based drug design, targeting some of the most critical diseases, such as some cancers [27–29], MASH [18–22], type 2 diabetes [23], and neurodegenerative diseases [24–26]. Nonetheless, many key questions remain that need to be addressed to understand this remarkable transporter fully (see Outstanding questions).

Outstanding questions

How did the MPC evolve, and what is its relationship with other members of the TOG superfamily?

How does pyruvate binding trigger conformational changes in the alternating access mechanism of MPC?

Are there other physiologically relevant substrates that may act as counter substrates for MPC to increase the re-orientation rate?

What are the molecular details of the proton coupling mechanism, and is it universal in different orthologs?

What are the binding poses of other major inhibitor classes? Do they all bind to the same site using similar principles? Do they all inhibit the same state?

What is the affinity of small-molecule inhibitors for MPCs from different species?

Can the determined structures be used to develop novel inhibitor classes using structure-based drug design?

Can novel inhibitors of MPC be used to treat some malignancies, type 2 diabetes, metabolic-associated steatohepatitis (MASH), neurodegenerative diseases, and alopecia?

Acknowledgments

This review was supported by the UKRI Medical Research Council (MC_UU_00028/2), the UKRI Biotechnology and Biological Sciences Research Council (BB/S00940X/1), and by the Division of Intramural Research of the National Institutes of Health (NIH), National Institute of Neurological Disorders and Stroke (NS003139). The content is solely the responsibility of the authors and does not necessarily represent the official views of the National Institutes of Health.

Declaration of interests

No conflicts of interest are declared.

Supplemental information

Supplemental information associated with this article can be found online at https://doi.org/10.1016/j.tibs.2025.11.002.

References

1. Merritt, M.E. *et al.* (2011) Flux through hepatic pyruvate carboxylase and phosphoenolpyruvate carboxykinase detected by hyperpolarized 13C magnetic resonance. *Proc. Natl. Acad. Sci. U. S. A.* 108, 19084–19089
2. Tavoulari, S. *et al.* (2023) Fifty years of the mitochondrial pyruvate carrier: new insights into its structure, function, and inhibition. *Acta Physiol. (Oxf.)* 238, e14016
3. Gray, L.R. *et al.* (2014) Regulation of pyruvate metabolism and human disease. *Cell Mol. Life Sci.* 71, 2577–2604
4. Buchanan, J.L. and Taylor, E.B. (2020) Mitochondrial pyruvate carrier function in health and disease across the lifespan. *Biomolecules* 10, 1162
5. Yiew, N.K.H. and Finck, B.N. (2022) The mitochondrial pyruvate carrier at the crossroads of intermediary metabolism. *Am. J. Physiol. Endocrinol. Metab.* 323, E33–E52
6. Zangari, J. *et al.* (2020) The multifaceted pyruvate metabolism: role of the mitochondrial pyruvate carrier. *Biomolecules* 10, 1068
7. Klingenberg, M. (1970) Mitochondria metabolite transport. *FEBS Lett.* 6, 145–154
8. Papa, S. *et al.* (1971) The transport of pyruvate in rat liver mitochondria. *FEBS Lett.* 12, 285–288
9. Papa, S. and Paradies, G. (1974) On the mechanism of translocation of pyruvate and other monocarboxylic acids in rat-liver mitochondria. *Eur. J. Biochem.* 49, 265–274
10. Halestrap, A.P. (1975) The mitochondrial pyruvate carrier. Kinetics and specificity for substrates and inhibitors. *Biochem. J.* 148, 85–96
11. Halestrap, A.P. (1976) The mechanism of the inhibition of the mitochondrial pyruvate transportater by alpha-cyanocinnamate derivatives. *Biochem. J.* 156, 181–183
12. Herzig, S. *et al.* (2012) Identification and functional expression of the mitochondrial pyruvate carrier. *Science* 337, 93–96
13. Bricker, D.K. *et al.* (2012) A mitochondrial pyruvate carrier required for pyruvate uptake in yeast, Drosophila, and humans. *Science* 337, 96–100
14. Tavoulari, S. *et al.* (2019) The yeast mitochondrial pyruvate carrier is a hetero-dimer in its functional state. *EMBO J.* 38, e100785
15. Tavoulari, S. *et al.* (2022) Key features of inhibitor binding to the human mitochondrial pyruvate carrier hetero-dimer. *Mol. Metab.* 60, 101469

16. Bender, T. *et al.* (2015) Regulation of mitochondrial pyruvate uptake by alternative pyruvate carrier complexes. *EMBO J.* 34, 911–924
17. Vanderperre, B. *et al.* (2016) MPC1-like is a placental mammal-specific mitochondrial pyruvate carrier subunit expressed in postmeiotic male germ cells. *J. Biol. Chem.* 291, 16448–16461
18. McCommis, K.S. *et al.* (2017) Targeting the mitochondrial pyruvate carrier attenuates fibrosis in a mouse model of nonalcoholic steatohepatitis. *Hepatology* 65, 1543–1556
19. Harrison, S.A. *et al.* (2020) Insulin sensitizer MSDC-0602K in non-alcoholic steatohepatitis: a randomized, double-blind, placebo-controlled phase IIb study. *J. Hepatol.* 72, 613–626
20. Colca, J.R. *et al.* (2018) MSDC-0602K, a metabolic modulator directed at the core pathology of non-alcoholic steatohepatitis. *Expert Opin. Investig. Drugs* 27, 631–636
21. Jacques, V. *et al.* (2021) Deuterium-stabilized (R)-pioglitazone (PXL065) is responsible for pioglitazone efficacy in NASH yet exhibits little to no PPARgamma activity. *Hepatol. Commun.* 5, 1412–1425
22. Harrison, S.A. *et al.* (2023) Evaluation of PXL065 – deuterium-stabilized (R)-pioglitazone in patients with NASH: a phase II randomized placebo-controlled trial (DESTINY-1). *J. Hepatol.* 78, 914–925
23. Hodges, W.T. *et al.* (2022) Mitochondrial pyruvate carrier inhibitors improve metabolic parameters in diet-induced obese mice. *J. Biol. Chem.* 298, 101554
24. Ghosh, A. *et al.* (2016) Mitochondrial pyruvate carrier regulates autophagy, inflammation, and neurodegeneration in experimental models of Parkinson's disease. *Sci. Transl. Med.* 8, 368ra174
25. Quansah, E. *et al.* (2018) Targeting energy metabolism via the mitochondrial pyruvate carrier as a novel approach to attenuate neurodegeneration. *Mol. Neurodegener.* 13, 28
26. Divakaruni, A.S. *et al.* (2017) Inhibition of the mitochondrial pyruvate carrier protects from excitotoxic neuronal death. *J. Cell. Biol.* 216, 1091–1105
27. Bader, D.A. *et al.* (2019) Mitochondrial pyruvate import is a metabolic vulnerability in androgen receptor-driven prostate cancer. *Nat. Metab.* 1, 70–85
28. Tompkins, S.C. *et al.* (2019) Disrupting mitochondrial pyruvate uptake directs glutamine into the TCA cycle away from glutathione synthesis and impairs hepatocellular tumorigenesis. *Cell Rep.* 28, 2608–2619 e6
29. Corbet, C. *et al.* (2018) Interruption of lactate uptake by inhibiting mitochondrial pyruvate transport unravels direct antitumor and radiosensitizing effects. *Nat. Commun.* 9, 1208
30. Du, J. *et al.* (2013) Inhibition of mitochondrial pyruvate transport by zaprinast causes massive accumulation of aspartate at the expense of glutamate in the retina. *J. Biol. Chem.* 288, 36129–36140
31. Nancolas, B. *et al.* (2016) The anti-tumour agent lonidamine is a potent inhibitor of the mitochondrial pyruvate carrier and plasma membrane monocarboxylate transporters. *Biochem. J.* 473, 929–936
32. Nath, K. *et al.* (2016) Mechanism of antineoplastic activity of lonidamine. *Biochim. Biophys. Acta* 1866, 151–162
33. Divakaruni, A.S. *et al.* (2013) Thiazolidinediones are acute, specific inhibitors of the mitochondrial pyruvate carrier. *Proc. Natl. Acad. Sci. U. S. A.* 110, 5422–5427
34. Hildyard, J.C. *et al.* (2005) Identification and characterisation of a new class of highly specific and potent inhibitors of the mitochondrial pyruvate carrier. *Biochim. Biophys. Acta* 1707, 221–230
35. Sichrovsky, M. *et al.* (2025) Molecular basis of pyruvate transport and inhibition of the human mitochondrial pyruvate carrier. *Sci. Adv.* 11, eadw1489
36. Liang, J. *et al.* (2025) Structures and mechanism of the human mitochondrial pyruvate carrier. *Nature* 641, 258–265
37. He, Z. *et al.* (2025) Structure of mitochondrial pyruvate carrier and its inhibition mechanism. *Nature* 641, 250–257
38. Sun, Y. *et al.* (2025) Structure of human mitochondrial pyruvate carrier MPC1 and MPC2 complex. *Nat. Commun.* 16, 6700
39. Rampelt, H. *et al.* (2020) The mitochondrial carrier pathway transports non-canonical substrates with an odd number of transmembrane segments. *BMC Biol.* 18, 2
40. Acoba, M.G. *et al.* (2021) The mitochondrial carrier SFXN1 is critical for complex III integrity and cellular metabolism. *Cell Rep.* 34, 108869
41. Henderson, R. (1995) The potential and limitations of neutrons, electrons and X-rays for atomic resolution microscopy of unstained biological molecules. *Q. Rev. Biophys.* 28, 171–193
42. Wentinck, K. *et al.* (2022) Putting on molecular weight: enabling cryo-EM structure determination of sub-100-kDa proteins. *Curr. Res. Struct. Biol.* 4, 332–337
43. Jakobi, A.J. *et al.* (2017) Model-based local density sharpening of cryo-EM maps. *Elife* 6, e27131
44. Botte, M. *et al.* (2022) Cryo-EM structures of a LptDE transporter in complex with pro-macrobodies offer insight into lipopolysaccharide translocation. *Nat. Commun.* 13, 1826
45. Medrano-Soto, A. *et al.* (2020) Expansion of the transporter-opsin-G protein-coupled receptor superfamily with five new protein families. *PLoS One* 15, e0231085
46. Han, L. *et al.* (2017) Molecular mechanism of substrate recognition and transport by the AtSWEET13 sugar transporter. *Proc. Natl. Acad. Sci. U. S. A.* 114, 10089–10094
47. Xu, Y. *et al.* (2014) Structures of bacterial homologues of SWEET transporters in two distinct conformations. *Nature* 515, 448–452
48. Lobel, M. *et al.* (2022) Structural basis for proton coupled cystine transport by cystinosin. *Nat. Commun.* 13, 4845
49. Brauer, P. *et al.* (2019) Structural basis for pH-dependent retrieval of ER proteins from the Golgi by the KDEL receptor. *Science* 363, 1103–1107
50. Youkharibache, P. *et al.* (2020) Pseudo-symmetric assembly of protodomains as a common denominator in the evolution of polytopic helical membrane proteins. *J. Mol. Evol.* 88, 319–344
51. Hegazy, L. *et al.* (2022) Identification of novel mitochondrial pyruvate carrier inhibitors by homology modeling and pharmacophore-based virtual screening. *Biomedicines* 10, 365
52. Springett, R. *et al.* (2017) Modelling the free energy profile of the mitochondrial ADP/ATP carrier. *Biochim. Biophys. Acta* 1858, 906–914
53. Rieger, B. *et al.* (2014) Lateral pH gradient between OXPHOS complex IV and F(0)F(1) ATP-synthase in folded mitochondrial membranes. *Nat. Commun.* 5, 3103
54. Strauss, M. *et al.* (2008) Dimer ribbons of ATP synthase shape the inner mitochondrial membrane. *Embo J.* 27, 1154–1160
55. Edgcomb, S.P. and Murphy, K.P. (2002) Variability in the pKa of histidine side-chains correlates with burial within proteins. *Proteins* 49, 1–6
56. Liu, T. *et al.* (1997) Determination of pKa values of the histidine side chains of phosphatidylinositol-specific phospholipase C from *Bacillus cereus* by NMR spectroscopy and site-directed mutagenesis. *Protein Sci.* 6, 1937–1944
57. Ancona, N. *et al.* (2023) PKAD-2: new entries and expansion of functionalities of the database of experimentally measured pKas of proteins. *J. Comput. Biophys. Chem.* 22, 515–524
58. Kazmier, K. *et al.* (2014) Conformational dynamics of ligand-dependent alternating access in LeuT. *Nat. Struct. Mol. Biol.* 21, 472–479
59. Kazmier, K. *et al.* (2014) Conformational cycle and ion-coupling mechanism of the Na+/hydantoin transporter Mhp1. *Proc. Natl. Acad. Sci. U. S. A.* 111, 14752–14757
60. Kazmier, K. *et al.* (2017) Alternating access mechanisms of LeuT-fold transporters: trailblazing towards the promised energy landscapes. *Curr. Opin. Struct. Biol.* 45, 100–108
61. Chen, Z. *et al.* (2012) Insulin resistance and metabolic derangements in obese mice are ameliorated by a novel peroxisome proliferator-activated receptor gamma-sparing thiazolidinedione. *J. Biol. Chem.* 287, 23537–23548
62. Colca, J.R. *et al.* (2014) Insulin sensitizers in 2013: new insights for the development of novel therapeutic agents to treat metabolic diseases. *Expert Opin. Investig. Drugs* 23, 1–7
63. Jamali, B. *et al.* (2004) Generic, highly selective and robust capillary electrophoresis method for separation of a racemic mixture of glitazone compounds. *J. Chromatogr. A* 1049, 183–187